Compact MMI-Based AWGs in a Scalable Monolithic Silicon Photonics Platform

Ayat M. Taha, Sujith Chandran, Jaime Viegas, Yusheng Bian, Michal Rakowski, Rod Augur, Ajey Jacob, and Marcus S. Dahlem

***Abstract*—We demonstrate a compact ($367 \times 67\ \mu m^2$) four-channel wavelength division multiplexer using an arrayed waveguide grating based on multimode interference couplers, and built on a monolithic silicon photonics platform. The design is particularly attractive due to the thin device layer. A semi-numerical approach was used for device design and simulation. Optical measurements were found to be consistent with simulation results. The device channel spacing, 3-dB bandwidth and crosstalk were measured to be 97 GHz, 87 GHz and 9.6 dB, respectively, for the designed wavelength of operation near 1310 nm.**

***Index Terms*—Arrayed waveguide grating, multimode interference coupler, monolithic platform, silicon-on-insulator, silicon photonics.**

I. Introduction

THE continuous growth in telecommunication traffic demands communication systems to be efficient, flexible, and high speed. Optical communication systems have attracted considerable interest due to their potential in meeting the ever-increasing bandwidth demand. In addition to the inherent ultrahigh bandwidth, optical communication offers wavelength-division multiplexing (WDM), which provides extra degrees of freedom to increase the channel capacity by multiplexing signals of different frequencies/wavelengths in a single optical waveguide. Silicon-based integrated optics technology has proven to be a prime approach that meets the optical communication requirements via miniaturized optical components and circuitry on a planar substrate [1].

Manuscript received May 9, 2021; revised June 24, 2021; accepted July 20, 2021. Date of publication July 26, 2021; date of current version August 11, 2021. This work was supported by Khalifa University/SRC Center of Excellence on Integrated Photonics, GRC task 2713.001. *(Corresponding authors: Ayat M. Taha; Yusheng Bian.)*

Ayat M. Taha and Jaime Viegas are with the Electrical Engineering and Computer Science Department, Khalifa University, Abu Dhabi 127788, UAE (e-mail: ayat.taha@ku.ac.ae; jaime.viegas@ku.ac.ae).

Sujith Chandran is with the Electrical Engineering and Computer Science Department, Khalifa University, Abu Dhabi 127788, UAE, and also with the Information Sciences Institute, Admiralty Way, Marina Del Rey, CA 90292 USA (e-mail: connectsujith@gmail.com).

Yusheng Bian, Michal Rakowski, and Rod Augur are with the GLOBALFOUNDRIES, Malta, NY 12020 USA (e-mail: yusheng.bian@globalfoundries.com; michal.rakowski@globalfoundries.com; rod.augur@globalfoundries.com).

Ajey Jacob is with the Information Sciences Institute, University of Southern California, Marina Del Rey, CA 90292 USA (e-mail: ajey@isi.edu).

Marcus S. Dahlem is with the Electrical Engineering and Computer Science Department, Khalifa University, Abu Dhabi 127788, UAE, and also with the IMEC, 3001 Leuven, Belgium (e-mail: Marcus.Dahlem@imec.be).

Digital Object Identifier 10.1109/JPHOT.2021.3099436

Several silicon-on-insulator (SOI) based photonic components such as Mach-Zehnder interferometers (MZIs) [2]–[4], arrayed waveguide gratings (AWGs) [5], [6], and microring resonators, have been demonstrated for WDM applications. Among them, ring resonator-based WDM filters are promising due to their compact footprint [7]–[10]. However, the temperature dependent spectral response of silicon waveguides is an adverse factor in its manufacturability [11]. In addition, the performance of ring resonators is strongly affected by fabrication-induced errors [12]. To obtain a wideband filter response, higher order ring filter configurations are often used [13]. The coupling conditions demand stringent fabrication requirements that are impractical in the absence of active elements such as heaters. Alternatively, filters based on MZIs offer wideband operation, but wavelength dependency of the directional couplers significantly influences the filter performance in terms of crosstalk/extinction-ratio. Furthermore, the large footprint of the device is a significant setback in MZI filters, as multiple stages need to be cascaded to multiplex/de-multiplex more channels. In contrast, filters based on AWGs are more attractive due to their simple design approach and compactness, particularly on silicon substrates. AWGs are recognized as the sole solution to multiplex hundreds of channels with very narrow channel spacing (DWDM applications). S. Cheung *et al.* [14] have demonstrated an AWG on an SOI platform with 512 output channels and channel spacing of 25 GHz. Conventional AWG structures use power splitters based on wavefront division using free propagation regions (FPRs) [15], [16]. The shortcomings of these power splitters are the following: higher insertion loss, non-uniform power splitting, stringent fabrication requirements, and large device footprint [17], [18]. Multimode interference (MMI) couplers are commonly known for their wavelength-independent and fabrication-tolerant performance, together with uniform splitting ratios [19]–[21]. Consequently, the replacement of FPR power splitters with MMI-based power splitters is considerably favored in terms of device footprint, uniform power distribution among the outputs, and fewer waveguide arrays. Hence, they are prone to less phase errors and high throughput (low loss) due to the self-imaging principle [20]. In addition, MMI coupler phase relations can be well estimated analytically, enabling MMI-based designs to be less computationally intensive.

In this work, we demonstrate an MMI-based four-channel AWG designed on a monolithic silicon photonics platform with a thin device layer [22]–[24]. The work supports that the studied

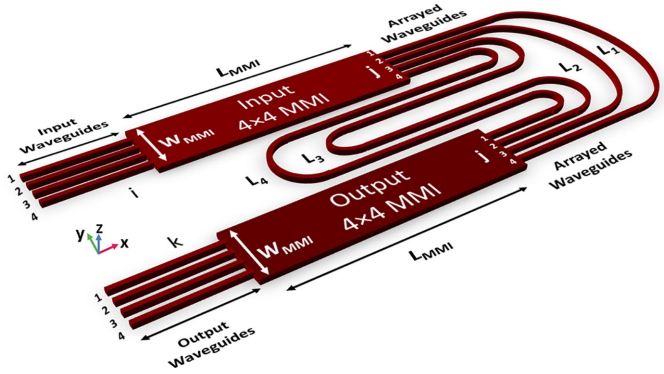

Fig. 1. Schematic perspective view of a 4×4 arrayed waveguide grating based on multimode interference couplers.

configuration can be further scaled for future technologies with improved performance figures.

II. Device Design and Simulation

From a footprint point of view, building AWGs in an SOI platform is preferred over other photonics platforms such as silica on silicon or lithium niobate [25], [26]. In comparison to AWGs based on the wavefront division, MMI-based AWGs can benefit from uniform power distribution, low loss power splitting, and a further reduction in the device footprint [20]. Moreover, the image resolution is significantly improved due to the self-imaging property of MMIs. A schematic illustration of the MMI-based AWG used in this work is shown in Fig. 1.

The device has three essential components: an input MMI that serves as a power splitter, single mode arrayed waveguides as the dispersive elements, and an output MMI coupler serving as a power combiner. Light launched from any input access waveguide (input waveguides are denoted by i_N) of the 4×4 MMI splitter is reproduced at each output waveguide (output waveguides of the input MMI splitter are denoted by j_N) in the form of multiple self-images with varying phase and uniform intensity distribution [20]. Light then propagates through the array of waveguides before reaching the output MMI coupler (output waveguides of the output MMI coupler are denoted by k_N). Due to the different lengths of the waveguides, light propagating in the array acquires different phases. Therefore, the length of the single-mode waveguides must be carefully designed such that the desired wavelengths interfere constructively at the various output ports of the MMI-based AWG with optimal spectral efficiency and resolution. A further consideration, to ascertain low crosstalk and symmetrical pattern of the multiple self-images, is the spacing of the MMI output ports and their positions in the MMI region. Therefore, the geometrical dimensions of the MMI coupler are crucial and must be carefully designed. In general, the access waveguides (input/output waveguides of the MMI coupler) are single-mode. However, waveguide tapers are used to interface the single-mode waveguides to the MMI section, resulting in better mode-matching at the interface and low-loss power coupling [27], [28].

The initial geometry of the 4×4 MMI coupler was designed using the well-known self-imaging principle [29]. To further optimize the design parameters, Lumerical FDTD and MODE Solutions simulation tools were used. Ideally, 3D FDTD simulations should be used for design optimization; however, due to the large footprint of the MMI couplers, it is more computationally intensive and time consuming. Therefore, Variational FDTD (varFDTD) was used for the parameter sweeps to optimize the device geometry. The device layer thickness, single-mode waveguide width, and sidewall angles are specific to the monolithic silicon photonic technology used in this work [24]. Relevant back end of line (BEOL) layers of the technology were also considered in the device simulation. As mentioned earlier, the MMI section was interfaced with tapered access waveguides, with a maximum width of 1.2 μm and a minimum width equal to the access waveguide width (350 nm). The length of the tapers was sufficient to ensure a smooth transition of the optical mode (15 μm). The width of the MMI splitter (W_{MMI}) was set to 6 μm to allow for the output ports of the MMI to be well separated (center-to-center separation of 1.58 μm) without any significant mode overlap/coupling. Simulation results showed an optimum MMI length (L_{MMI}) of 79 μm. Fig. 2(a) depicts the simulated top view of the 4×4 MMI coupler ($L_{MMI} = 79$ μm and $W_{MMI} = 6$ μm) when input port 2 (i_2) is excited with TE polarized light at a wavelength of 1310 nm. The AWG design is optimized for TE polarization as the waveguide geometry and other photonics components (bends, splitters, grating couplers, etc.) in GLOBALFOUNDRIES process design kit (PDK) are optimized for the same polarization. The waveguide configuration allows higher confinement for TE modes and the fabricated vertical grating couplers were also designed specifically for TE mode operation.The AWG device was designed for 100 GHz channel spacing to be operating near the wavelength of 1310 nm (O-band) as the fabrication technology (GLOBALFOUNDRIES) is optimized for this wavelength. To verify the accuracy of the varFDTD simulation results, the optimum geometry simulation was repeated using 3D FDTD, and the results are presented in Fig. 2(b). The comparison clearly shows the agreement between 3D FDTD and varFDTD, which validated the use of the latter for further optimization of the complete device. The excess loss of the optimum design was simulated to be 0.66 dB, and the maximum non-uniformity was estimated to be 0.78 dB. Fig. 2(c) shows the simulated (normalized) wavelength-dependent output response of the MMI splitter for various input excitation ports. The normalization of the results was performed for each port by taking the ratio of the transmission in the respective port to the total output transmission (sum of the transmission in all output ports). Given that the design is based on a thin device layer, realizing a wavelength independent response over the entire O-band is challenging. Therefore, the device response was optimized for an operating wavelength near 1310 nm. Simulation results in Fig. 2(c) show that the splitting ratio stays nearly 0.25 for all output ports at wavelengths near 1310 nm.

An important factor in the MMI-based AWG design is the arrayed waveguide length estimation. The relative phase between the arrayed waveguides, in conjunction with the self-imaging induced phase at the output of MMI couplers, is critical in

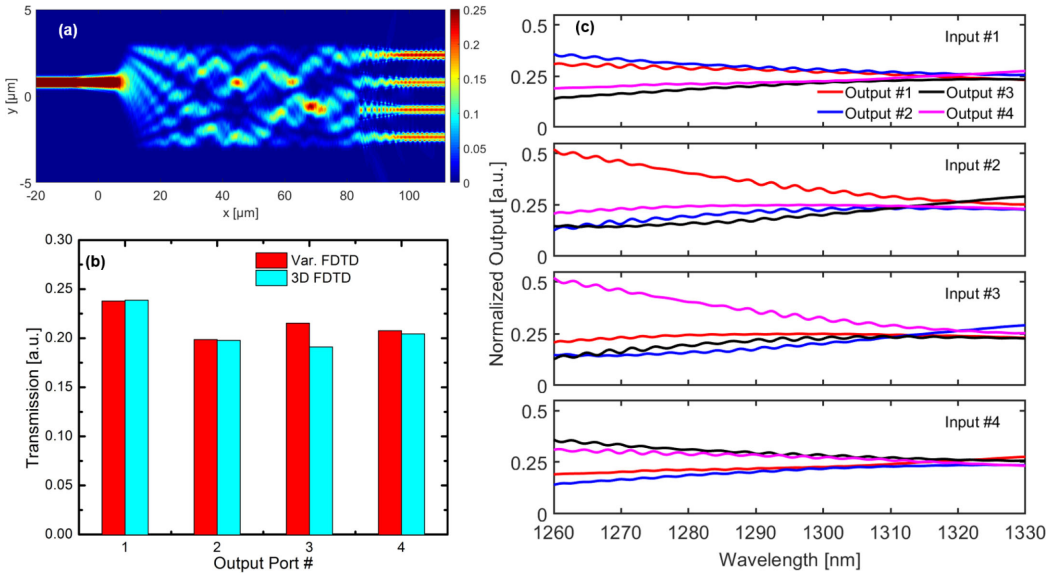

Fig. 2. Variational FDTD simulation results: (a) top-view of the 4×4 input MMI coupler with length $= 79$ μm and width $= 6$ μm, when input port #2 is excited with a TE-polarized source of wavelength 1310 nm; (b) comparison of the simulated transmission obtained at various output ports for varFDTD and 3D FDTD; and (c) wavelength-dependent transmission (normalized) of the 4×4 MMI coupler, for excitation at the various input ports.

optimizing the array length of the AWGs. In this study, in order to obtain a compact device footprint, the second arm (L_2) was set as the shortest and as the reference arm of the array [29]. Setting the first or the last waveguide in the array as the reference arm would result in higher crosstalk and significantly longer arms. Moreover, to achieve a nearly symmetrical pattern of the self-images, the reference arm selection is limited to L_2 or L_3 in a 4×4 AWG. In contrast to the FPR-based power splitter, the MMI-based power splitters introduce a non-uniform phase among the output ports [29]. As a consequence, the length of the arrayed waveguides must be designed such that the additional phase difference is balanced out. Therefore, an array arm factor (d_j) is used to estimate the length of the arrayed waveguides for phase compensation, as well as ensuring no overlapping in the arrays [29]:

$$L_j \approx L_m + d_j \Delta L, \tag{1}$$

where ΔL is the length difference required to obtain a phase delay of $2\pi/N$ between the adjacent wavelength channels, L_m the reference arm, and d_j an integer number. The following formalism shows the steps needed to calculate the length of the arrayed waveguides such that the respective phase delays of each arm, along with the phase of the self-imaged output from the input MMI splitter, result in a constructive interference at the output of the 4×4 AWG-based WDM. The phase at the output of the input MMI splitter j_N, attributed by input i_N, is defined by [29]:

$$\phi_{i,j} = \phi_1 - \frac{\pi}{2}(-1)^{i+j+N} + \frac{\pi}{4N} \times \left[i + j - i^2 - j^2 + (-1)^{i+j+N} \left(2ij - i - j + \frac{1}{2} \right) \right], \tag{2}$$

where ϕ_1 is a constant phase. The phase difference between j_N and k_N (see Fig. 1) with respect to the reference input, which we define here as m, is calculated by [29]:

$$\Delta\phi_{i,j} = \frac{\pi(-1)^N}{2N} \left\{ \left[(-1)^{j+m} \left(j - \frac{1}{2} \right) - \left(m - \frac{1}{2} \right) \right] \times \left[(-1)^{k+m} \left(k - \frac{1}{2} \right) - \left(m - \frac{1}{2} \right) \right] \right\} - \frac{\pi(-1)^N}{2} \left\{ \left[1 - (-1)^{j+m} - (-1)^{k+m} + (-1)^{j+k} \right] \right\}, \tag{3}$$

where $\phi_{j,k}$ is a multiple of $2\pi/N$, which is the phase shift separating neighboring wavelength channels. Subsequently, the phase of the array arms which compensates for the transfer phase of the MMI splitter is given by [29]:

$$\psi_{j,k} = \left[-\frac{N}{2\pi} \Delta\phi_{j,k} \right] \bmod(N), \tag{4}$$

where the modulus operator is used to restrict the result of $\psi_{j,k}$ to a range between 0 and $N - 1$. Finally, the array arm factor is calculated using the following equation [29]:

$$d_j = \psi_{j,k} + B_j N, \tag{5}$$

where the term B_j is the smallest integer number that prevents intersection/crossing between adjacent waveguides in the array. As mentioned, the reference arm was selected to be the second arm; using Eqs. 3 and 4, $\psi_{j,k}$ was calculated for $m = 2$, and the respective values are shown in Table I. From the table, it is seen that in the case of output k_1, the phase $\psi_{j,k}$ at the fourth arm (j_4) was calculated to be less than the phase at arm j_3. Therefore, the computed array arm factor d_4 was less than d_3 for B_4 equal to unity. Accordingly, the term B_4 (5) needs to be incremented in order to increase d_4 and avoid intersection between the two arms.

TABLE I
CALCULATED VALUES OF $\psi_{j,k}$ FOR $m = 2$ IN A 4×4 MMI COUPLER

	j_1	j_2	j_3	j_4
$k1$	3	0	2	1
$k2$	0	0	0	0
$k3$	2	0	0	2
$k4$	1	0	2	3

TABLE II
OPTIMUM VALUES OF d_j FOR THE 4×4 AWG-BASED WDM

	d_1	d_2	d_3	d_4	d_{max}
$k1$	3	0	2	5	5
$k2$	0	0	0	0	-
$k3$	2	0	4	6	6
$k4$	1	0	2	3	3

TABLE III
CALCULATED LENGTHS OF THE ARRAYED WAVEGUIDES, WITH THE SECOND ARM SET AS THE REFERENCE ARM OF THE ARRAY

Array #	Length (μm)
1	275.66
2	100
3	450.32
4	625.98

However, the goal is to find the best combination of $\psi_{j,k}$ values for $m = 2$ that would prompt the smallest d_j values, hence the shortest combination of arm lengths of the array. The optimum values of d_j are shown in Table II, and the selected set of d_j values is the one for output k_4, for which the calculated d_{max} is the smallest.

To ensure compact routing of the waveguide array, the reference arm length was set to be 100 μm, and the differential length (ΔL) of the other waveguides in the array was then estimated using (1) as [29]:

$$\Delta L = \frac{\lambda_0(\lambda_0 + \Delta\lambda)}{N\,\Delta\lambda n_g}, \tag{6}$$

where λ_0 is the center wavelength, $\Delta\lambda$ the channel spacing around 1310 nm (which in this case is 0.572 nm, corresponding to 100 GHz), N the number of access waveguides, and n_g the group index of the arrayed waveguides. The lengths of the arrayed waveguides were then derived using (1), and are shown in Table III. To obtain the complete simulation response of the AWG, the output MMI coupler was evaluated as follows. A mode source was placed at each input port of the input MMI splitter. The recorded intensities and phases from the output waveguides of the input MMI splitter were then used as sources at each input waveguide of the output MMI coupler. The phase delay associated with the different lengths of the AWG arms was also accounted for in the simulation, by introducing an offset to every input source, which results in launching each source at different times. The corresponding offset was calculated using the following expression:

$$T_j = \frac{L_j}{v_g}, \tag{7}$$

where T_j is the offset (time delay), L_j the length of the array arms, and v_g the group velocity of the single-mode arrayed waveguides. The spectral transmission of the AWG-based WDM is shown in Fig. 3. The four different channels are conspicuous,

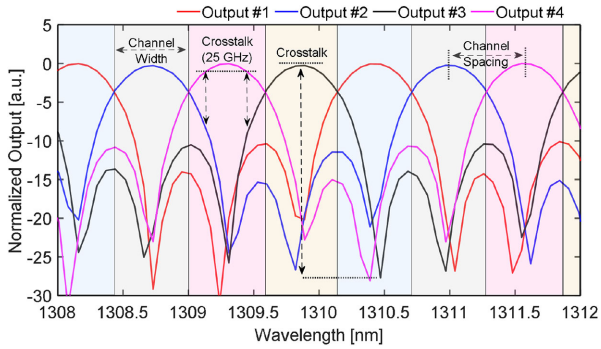

Fig. 3. Spectral transmission of the four-channel WDM, with channel spacing of 100 GHz. The spectral response at all four outputs is shown for excitation at input #2 of the input MMI splitter.

where good uniformity and low side lobes are observed within adjacent channels. Simulation results show that the channel spacing and the 3-dB optical bandwidth are around 100 GHz, and that the device has low crosstalk (20–25 dB) and a crosstalk at 25 GHz channel bandwidth ranging from 12–15 dB, making it suitable for operating as a wavelength-division multiplexer. This confirms that the selected access waveguide separation was sufficient to mitigate crosstalk between neighboring channels, thus enhancing the extinction ratio of the spectral response. Crosstalk is defined as the ratio of the power level (in dB) of the desired channel to the adjacent channel, measured from the waveguide port designed to drop the desired channel. The power levels were measured at the center wavelength of each channel.

III. FABRICATION AND CHARACTERIZATION

GDS layouts with the optimum device geometries were prepared based on a monolithic silicon photonics technology [24]. Grating couplers were used at the input and output ends of the devices. Optical characterization was conducted using an O-band tunable laser source and a broadband photodetector. The light from the tunable laser was coupled to the input grating coupler through an inline-polarization controller. The polarization controller was used to align the input light to TE polarization. At the output of the device, light was collected using another grating coupler and fed to the photodetector. Both laser and photodetector were interfaced using LabVIEW to automatically acquire the wavelength-dependent response of the device under test. Fig. 4 shows the measured wavelength-dependent transmission of the 4×4 input MMI splitters when various input ports were excited. Fig. 4(a) and (b) correspond to different MMIs lengths (79 μm and 80 μm, respectively). The width of the MMI was designed to be 6 μm for both devices. The transmission is normalized such that the total output power (sum of all four output ports) is unity. The oscillations in the measured transmission curves are likely due to reflections, and were also observed in the theoretical plots in Fig. 2(c). The measured transmission shows a significant wavelength dependency over the entire O-band, apart from the region near the desired wavelength ($\lambda = 1310$ nm), where the splitting ratio remains close to 0.25 for both devices. The experimental results were in good agreement with

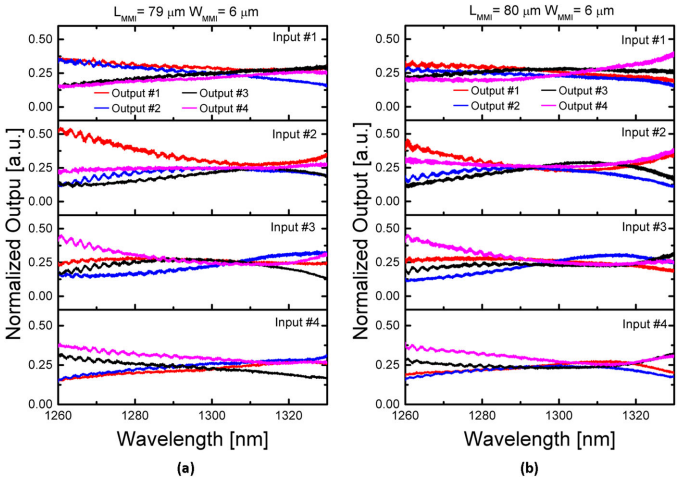

Fig. 4. Wavelength-dependent transmission measured at all output ports, for excitation at various input ports of the devices with: (a) $L_{MMI} = 79$ μm; and (b) $L_{MMI} = 80$ μm. The MMI width was set to 6 μm for both devices.

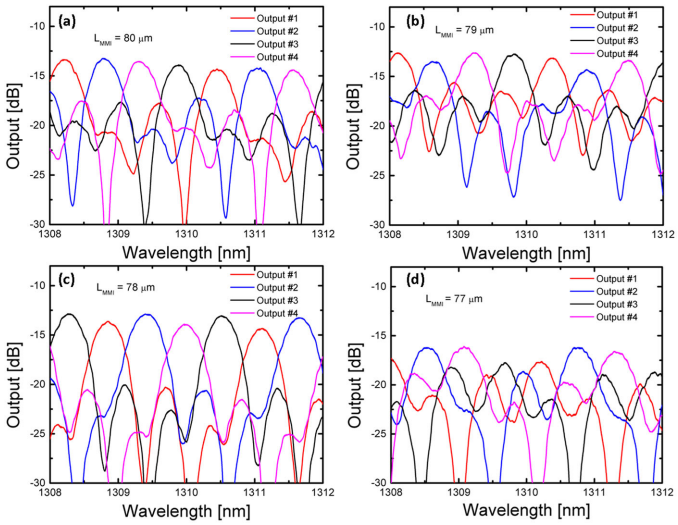

Fig. 5. Transmission spectra of the arrayed waveguide gratings, for excitation at input #2, with: (a) $L_{MMI} = 80$ μm; (b) $L_{MMI} = 79$ μm; (c) $L_{MMI} = 78$ μm; and (d) $L_{MMI} = 77$ μm.

the simulated curves, thus validating the varFDTD simulation analysis performed on both devices. A small wavelength shift was observed in the measured transmission between the two devices in Fig. 4, which was expected due to the minor difference in the MMI length.

Fig. 5 shows the transmission spectra around 1310 nm for a four-channel AWG with various MMI lengths, for excitation at input #2. Four different designs were studied in this work, with $L_{MMI} = 80$ μm, 79 μm, 78 μm, and 77 μm, for Design #1 to Design #4, respectively. The other AWG parameters, including the MMI width (6 μm) and arrayed waveguide lengths, were kept constant for all four designs. Each measured spectrum incorporates the response from the grating couplers positioned at the input and output of the devices. It is evident from Fig. 5 that the output response of the AWG depends on the length of the MMI couplers. Simulation results were found to be optimum for the design with $L_{MMI} = 79$ μm (Design #2); however, experimental results indicate that the best performance was achieved for the design with $L_{MMI} = 78$ μm (Design #3).

TABLE IV
SUMMARY OF THE MEASURED PERFORMANCE OF THE FOUR DEVICES NEAR THE DESIGN WAVELENGTH OF $\lambda = 1310$ NM

Device	MMI Length [μm]	Chanel separation [GHz]	3-dB bandwidth [GHz]	Crosstalk [dB]
Design #1	80	90 - 104	86 - 87	7.0 - 7.3
Design #2	79	88 - 104	85 - 94	4.3 - 5.8
Design #3	78	94 - 102	87 - 94	9.6 - 12.6
Design #4	77	94 - 101	85 - 99	2.2 - 6.0

The measured results of the four AWG designs are summarized in Table IV. The channel spacing varies between 88–104 GHz for Design #2, close to the target spacing (100 GHz). The slight variation in the channel spacing is attributed to phase errors in the waveguide array. For the best performing device (Design #3, with $L_{MMI} = 78$ μm), the measured channel spacing varies between 94–102 GHz, with channel bandwidth between 87–94 GHz and crosstalk between 9.6–12.6 dB. The crosstalk at 25 GHz bandwidth was measured to be ranging from 7.6–11.4 dB. The device was designed to have a channel center wavelength of around 1310 nm, however a channel drift of around 0.2 nm was observed in the experimental spectrum.

The small deviations between simulated and experimental results can be attributed to two main factors: (i) the full simulation was done in parts due to the large footprint of the device; and (ii) small variations of the geometrical parameters in the fabricated devices (compared to design), which translates to phase errors. The deterioration of the extinction ratio results from the non-uniform splitting at the output ports of the MMIs. As shown in Fig. 4, the splitting ratio of the MMI with $L_{MMI} = 80$ μm was nearly uniform around 1310 nm, while for the device with $L_{MMI} = 79$ μm the splitting was uneven. This non-uniformity explains why the optical performance of the device with $L_{MMI} = 80$ μm was better than Design #2 (as also seen in Table IV). Further optimization of the minimum waveguide separation is needed for reducing channel crosstalk. Fine-tuning of the MMI splitter geometry and the position of the access waveguides can also improve the power splitting uniformity, and therefore further improve the performance of the 4×4 MMI. Additionally, multistage designs can achieve lower crosstalk at the expense of device footprint [30].

IV. CONCLUSION

In summary, we design and demonstrate a compact four-channel wavelength-division multiplexer using an AWG based on MMI couplers. Despite the compactness of the device, high-quality results were achieved. The MMI couplers have tapered input and output access waveguides to reduce back reflections and the overall insertion loss. The device was designed for a 100 GHz channel spacing in a 4-channel WDM, a 3-dB optical bandwidth of about 87 GHz, high channel uniformity, and excess loss less than 1 dB for the MMI couplers. The best measured performance was for the device with MMI lengths of 78 μm (and a width of 6 μm). A maximum crosstalk up to 12.7 dB

was measured for this design. The performance can be further enhanced by improving the power splitting uniformity of the MMI couplers, particularly by optimizing the access waveguide separation and orientation. Ideally, the proposed device can be extended to multiplex hundreds of channels. However, increasing the number of channels result in a non-uniform power splitting and hence increasing the crosstalk between adjacent channels. In order to extend the device performance to support several channels, it would require increasing the number of MMI waveguide input/output ports with optimal power splitting characteristics.

ACKNOWLEDGMENT

The authors thank GLOBALFOUNDRIES for providing silicon fabrication through the MPW university program.

REFERENCES

[1] Q. Cheng, M. Bahadori, M. Glick, S. Rumley, and K. Bergman, "Recent advances in optical technologies for data centers: A review," *Optica*, vol. 5, no. 11, pp. 1354–1370, 2018.

[2] F. Horst, W. M. Green, S. Assefa, S. M. Shank, Y. A. Vlasov, and B. J. Offrein, "Cascaded mach-zehnder wavelength filters in silicon photonics for low loss and flat pass-band WDM (de-) multiplexing," *Opt. Exp.*, vol. 21, no. 10, pp. 11652–11658, 2013.

[3] A. Tervonen, P. Poyhonen, S. Honkanen, and M. Tahkokorpi, "A guided-wave Mach-Zehnder interferometer structure for wavelength multiplexing," *IEEE Photon. Technol. Lett.*, vol. 3, no. 6, pp. 516–518, Jun. 1991.

[4] S. Dwivedi, H. D'heer, and W. Bogaerts, "Maximizing fabrication and thermal tolerances of all-silicon FIR wavelength filters," *IEEE Photon. Technol. Lett.*, vol. 27, no. 8, pp. 871–874, Apr. 2015.

[5] J. Wang, S. Chen, and D. Dai, "Silicon hybrid demultiplexer with 64 channels for wavelength/mode-division multiplexed on-chip optical interconnects," *Opt. Lett.*, vol. 39, no. 24, pp. 6993–6996, 2014.

[6] A. Sugita, A. Kaneko, K. Okamoto, M. Itoh, A. Himeno, and Y. Ohmori, "Very low insertion loss arrayed-waveguide grating with vertically tapered waveguides," *IEEE Photon. Technol. Lett.*, vol. 12, no. 9, pp. 1180–1182, Sep. 2000.

[7] W. Bogaerts *et al.*, "Compact wavelength-selective functions in silicon-on-insulator photonic wires," *IEEE J. Sel. Topics Quantum Electron.*, vol. 12, no. 6, pp. 1394–1401, Nov./Dec. 2006.

[8] H. Jayatilleka, K. Murray, M. Caverley, N. A. Jaeger, L. Chrostowski, and S. Shekhar, "Crosstalk in SOI microring resonator-based filters," *J. Lightw. Technol.*, vol. 34, no. 12, pp. 2886–2896, 2015.

[9] T. Sreenivasulu *et al.*, "Photonic crystal ring resonator-based four-channel dense wavelength division multiplexing demultiplexer on silicon on insulator platform: Design and analysis," *Opt. Eng.*, vol. 57, no. 4, p. 046109, 2018.

[10] D. Tan, A. Grieco, and Y. Fainman, "Towards 100 channel dense wavelength division multiplexing with 100 GHz spacing on silicon," *Opt. Exp.*, vol. 22, no. 9, pp. 10408–10415, 2014.

[11] X. Zheng *et al.*, "A tunable 1×4 silicon cmos photonic wavelength multiplexer/demultiplexer for dense optical interconnects," *Opt. Exp.*, vol. 18, no. 5, pp. 5151–5160, 2010.

[12] M. S. Dahlem, C. W. Holzwarth, A. Khilo, F. X. Kärtner, H. I. Smith, and E. P. Ippen, "Reconfigurable multi-channel second-order silicon microring-resonator filterbanks for on-chip WDM systems," *Opt. Exp.*, vol. 19, no. 1, pp. 306–316, 2011.

[13] M. A. Popovic *et al.*, "Tunable, fourth-order silicon microring-resonator add-drop filters," in *Proc. 33rd Eur. Conf. Exhib. Opt. Commun.*, 2007, pp. 1–2.

[14] S. Cheung, T. Su, K. Okamoto, and S. Yoo, "Ultra-compact silicon photonic $512\times$ 512 25 GHz arrayed waveguide grating router," *IEEE J. Sel. Topics Quantum Electron.*, vol. 20, no. 4, pp. 310–316, Jul./Aug. 2014.

[15] S. Pathak, M. Vanslembrouck, P. Dumon, D. Van Thourhout, and W. Bogaerts, "Optimized silicon AWG with flattened spectral response using an MMI aperture," *J. Lightw. Technol.*, vol. 31, no. 1, pp. 87–93, 2013.

[16] S. Pathak, D. Van Thourhout, and W. Bogaerts, "Design trade-offs for silicon-on-insulator-based AWGS for (de) multiplexer applications," *Opt. Lett.*, vol. 38, no. 16, pp. 2961–2964, 2013.

[17] J. Wang *et al.*, "Low-loss and low-crosstalk 8×8 silicon nanowire awg routers fabricated with cmos technology," *Opt. Exp.*, vol. 22, no. 8, pp. 9395–9403, 2014.

[18] S. Pathak, M. Vanslembrouck, P. Dumon, D. Van Thourhout, and W. Bogaerts, "Compact SOI-based polarization diversity wavelength demultiplexer circuit using two symmetric awgs," *Opt. Exp.*, vol. 20, no. 26, pp. B493–B500, 2012.

[19] M. Bachmann, P. A. Besse, and H. Melchior, "General self-imaging properties in $n \times n$ multimode interference couplers including phase relations," *Appl. Opt.*, vol. 33, no. 18, pp. 3905–3911, 1994.

[20] L. B. Soldano and E. C. Pennings, "Optical multi-mode interference devices based on self-imaging: Principles and applications," *J. Lightw. Technol.*, vol. 13, no. 4, pp. 615–627, 1995.

[21] A. Maese-Novo *et al.*, "Wavelength independent multimode interference coupler," *Opt. Exp.*, vol. 21, no. 6, pp. 7033–7040, 2013.

[22] S. Chandran *et al.*, "Beam shaping for ultra-compact waveguide crossings on monolithic silicon photonics platform," *Opt. Lett.*, vol. 45, no. 22, pp. 6230–6233, 2020.

[23] M. Rakowski *et al.*, "45 nm CMOS-silicon photonics monolithic technology (45CLO) for next-generation, low power and high speed optical interconnects," in *Proc. Opt. Fiber Commun. Conf. Opt. Soc. Amer.*, 2020, pp. T3H-3.

[24] K. Giewont *et al.*, "300-mm monolithic silicon photonics foundry technology," *IEEE J. Sel. Topics Quantum Electron.*, vol. 25, no. 5, pp. 1–11, Sep./Oct. 2019.

[25] M. Kawachi, "Recent progress in silica-based planar lightwave circuits on silicon," *IEE Proc.-Optoelectron.*, vol. 143, no. 5, pp. 257–262, 1996.

[26] M. Bazzan and C. Sada, "Optical waveguides in lithium niobate: Recent developments and applications," *Appl. Phys. Rev.*, vol. 2, no. 4, p. 040603, 2015.

[27] C.-D. Truong, M.-C. Nguyen, D.-T. Le, and T.-T. Le, "All-optical switch based on 1×3 multimode interference couplers," *Opt. Switching Netw.*, vol. 22, pp. 129–134, 2016.

[28] R. Halir *et al.*, "A design procedure for high-performance, rib-waveguide-based multimode interference couplers in silicon-on-insulator," *J. Lightw. Technol.*, vol. 26, no. 16, pp. 2928–2936, 2008.

[29] M. R. Paiam and R. I. MacDonald, "Design of phased-array wavelength division multiplexers using multimode interference couplers," *Appl. Opt.*, vol. 36, no. 21, pp. 5097–5108, 1997.

[30] B.-C. Lin, "Advanced crosstalk reduction in an $n \times n$ two-stage AWG-based switch with odd n," *Optik*, vol. 225, p. 165656, 2021.